Prediction of wetting condition in a reservoir rock using coupled digital rock and molecular dynamics simulation

Ashraful Islam, Joshua D. Moore, Rafael Salazar-Tio, Guangyuan Sun, Andrew Fager, Bernd Crouse, Sabine Schweizer, Kwan Skinner, Lalitha Subramanian

Dassault Systémes, Johnston, RI

Abstract. Wettability is one of the key inputs for digital rock simulations to calculate multiphase fluid transport properties. Reservoir rocks have spatially varying wettability that depends on local pressure, temperature, surface roughness, and mineral and fluid compositions. Here, a multiphase lattice Boltzmann method (LBM) is used to simulate a capillary pressure drainage simulation in an initially water-wet Berea sandstone, utilizing wettability inputs derived from fully atomistic molecular dynamics simulations. When oil invades the pore space as the capillary pressure is increased, a fraction of the pore-grain surface is altered from a water-wet to an oil-wet condition. The eligibility for alteration takes into account local capillary pressure, disjoining pressure, and micro-scale surface roughness. Wettability inputs to the multiphase simulation are contact angles, calculated from molecular dynamics simulations of oil droplets on mineral surfaces with hydrophilic and hydrophobic surface chemistry. The multiphase workflow demonstrates an iterative process where wettability is altered along with quasi-static fluid flow resulting in spatially varying wetting conditions of the simulated rock sample. The study investigates the slow dynamics of oil invasion and wettability alteration, taking into account the micro-scale pore shape dependence of the rock. The wettability distributions are compared with an image-based geometric intrusion analysis which mimics mercury intrusion porosimetry. The resulting wettability distribution holds the potential to enhance the realistic prediction of transport properties under in-situ reservoir conditions.

1 Introduction

Wettability is a measure of a fluid's tendency to adhere to a solid surface in the presence of other fluids. In the context of reservoir rocks, wettability plays a crucial role in determining fluid behavior and consequently the efficiency of oil and gas extraction. Reservoir rocks are usually composed of various minerals, such as quartz, clays, carbonates etc., that have various affinities toward fluids like oil, brine and others. The wettability of the rock determines how these fluids are distributed within the pore space and their ability to flow through the rock. As a result, wettability can significantly impact multiphase fluid displacement in a reservoir as well as capillary pressure and relative permeability experiments [1-5].

Typically, the wettability of a reservoir rock can be determined through various laboratory tests such as contact angle measurements, the Amott-Harvey method, the USBM method, and spontaneous imbibition [6]. Wettability tests are conducted in a controlled laboratory environment to replicate reservoir conditions and require access to facilities equipped with specialized instruments and expertise. Reservoir rocks, unlike man-made materials, tend to have spatially varying wettability, i.e., the contact angle varies from location to location on the surface of the grains in contact with the fluids in the pore space of a rock [7-9]. Thus, proper wettability characterization requires multiple samples across the reservoir to test. Obtaining representative rock samples from the reservoir for wettability testing can be a time-consuming process. It involves drilling multiple core samples, preserving their integrity, and preparing them for laboratory testing. Consequently, obtaining wettability data in a timely manner can sometimes be challenging for oil and gas operators.

With the advancement of imaging, such as x-ray micro-tomography (microCT) and computational fluid dynamics, it is now possible to perform special core analysis studies such as relative permeability or capillary pressure analysis digitally for the rock samples. Digital rock simulations offer certain benefits such as non-destructive analysis, allowing the user to perform what-if studies for the same sample, uncertainty quantifications, and above all else, reduced turnaround time. However, wettability is still needed as an input for relative permeability and capillary pressure simulations.

Digital imaging of rock samples by microCT or FIB-SEM can also help to determine the wettability of a reservoir rock without relying solely on laboratory testing. By imaging rock samples in the presence of various fluid phases and analyzing those using 3D image processing tools, one can calculate contact angles [10-15]. Observations of the relative fluid coverage of rock mineral surfaces can also be used to create a 3D map of the wetting state of the rock [7-8]. However, these procedures still require several weeks of laboratory "aging", which involves cleaning samples, followed by a "drainage" procedure where oil is pushed into the rock

---

sample filled with brine and aged for few weeks. Recently, a complementary numerical procedure to mimic aging was proposed [21]. However, the underlying molecular mechanisms for obtaining spatially variant wettability distributions was lacking in that initial approach.

Determining wettability and the initial fluid distribution using digital rock simulations is a complicated and challenging problem that spans the molecular to micro-scales. When oil intrudes the brine-filled pore space for the first time, the grains are usually coated with a thin water film. For the oil to be in contact with the grains, this film needs to be ruptured, which can be described by the disjoining pressure theory [16-18]. At the micro-scale, pore shape, curvature and surface roughness are critical to determining whether the water film can be ruptured. Afterwards, based on the pore fluid pressure, temperature, and fluid and mineral compositions, oil can create another layer on the initially water-wet surface and make the surface oil-wet. At the molecular scale, surface chemistry, temperature, pressure, and salinity play a major role in the wettability of mineral surfaces [19]. For example, the concentration of silanol (-SiOH) functional groups on quartz mineral surfaces can determine whether the wettability conditions are water-wet or oil-wet, and surface hydrophobicity may be increased through alkylation by organics present in oil reservoirs and rock formations [20]. Thus, both molecularly driven physicochemical properties and micro-scale multiphase fluid flow play an important role in reservoir rock wettability.

In a previous study [21], a numerical methodology for wettability alteration was implemented using a multiphase lattice Boltzmann method, utilizing a given disjoining pressure isotherm and assuming certain contact angles for the oil-wet and water-wet conditions. The initial workflow showcased an iterative process for wettability alteration, focusing on the force balance between curvature-based, applied, and disjoining pressures. That study [21] also discussed the possibility of extending the workflow using molecular dynamics simulations. Building upon this framework, the current work integrates the wettability alteration CFD workflow with molecular dynamics simulations of three-phase wettability models [22] of oil droplets in brine on mineral surfaces. In particular, we simulated the change in contact angle of an oil/brine/quartz system when the quartz surface transforms from a water-wet to an oil-wet condition under in-situ reservoir conditions using molecular dynamics. The computed contact angles are provided as inputs to the multiphase LBM simulation, whereas in previous work [21] they were assumed.

In this work, we describe a numerical digital rock workflow starting from pore-scale 3D image acquisition to fluid flow simulation, including a previously demonstrated wettability alteration process. Wettability alteration is carried out in a digitally reconstructed 3D pore-grain model, considering micro-scale interactions. In parallel, molecular dynamics simulations are performed at the reservoir pressure and temperature for oil droplets in brine on mineral surfaces to calculate contact angles. The resulting contact angles are used in multiphase pore-scale fluid flow simulations to obtain spatial distributions of fluid wettability. A molecular

mechanism for wettability alteration is considered by substituting functional groups capping the mineral surface, from hydroxyl groups (-OH) in the presence of water to alkyl groups ($-C_nH_{2n+1}$) as oil intrudes into the pores. As the oil-water interface moves along the mineral surface, this functional group substitution ultimately triggers the wettability alteration, as contact angles change from water-wet to oil-wet, shown later in this paper.

The following section describes the molecular dynamics and multiphase fluid flow simulation methodologies, followed by a description of the workflow for the coupling of these two scales, along with details of the wettability alteration method. Results from molecular dynamics and multiphase fluid simulations are then discussed, followed by the conclusions and a discussion of future research directions.

2 Methodology

2.1 Molecular dynamics simulation

Molecular dynamics (MD) simulations model atoms and molecules as interacting particles. The basic approach to all-atom MD involves solving Newton's second law for every atom in the simulation, where atomic forces are determined by an intermolecular force field, which describes van der Waals forces, electrostatic interactions, and chemical bonding between different atoms in the simulation [23]. Pressure and temperature can be controlled through thermostats and barostats [24]. Since the force field inherently takes into account the chemistry of the atoms and molecules, its development typically involves quantum mechanical calculations as well as rigorous benchmarking against experimental data, and these force fields can be used for a range of materials and conditions. For an MD run, the chemistry of the materials involved, their specific formulation and processing conditions, if applicable, is all that is needed. Experimental data is not utilized for performing MD simulations. By comparing system behaviour or properties (such as density, viscosity, diffusivity, miscibility, moduli, and stress-strain curves) calculated from MD simulations against experimentally measured lab data, molecular dynamics results are rigorously validated. With over six decades [25] of research and development on applications of MD simulations, it has become a mainstay in geochemistry, catalyst design, polymerization reaction optimization, and sustainable innovation.

Since this technique is applicable to systems made up of any element in the periodic table, it applies to a wide range of topics. In the energy industry, specifically in the oil and gas upstream sector, molecular dynamics simulations are used to study extraction, transport and processing of hydrocarbons. Design and optimization of fracturing fluids, gaining key insights into scale and hydrate formation [26], studying the aggregation behaviour of asphaltenes [27], and optimizing sustainable and green catalysts [28] for oil refining are a few examples where molecular dynamics simulations have been

successfully applied. In the area of sustainability, molecular dynamics simulations have been used to investigate CO_2 absorption in porous materials such as MOFs [29, 30] and zeolites [30], as well as in rocks and cement [31]. Critical phenomena such as CO_2 dissolution in brine present in reservoir rocks [32], supercritical CO_2 impact on degradation and ageing of elastomer [33] completion tools can also be simulated. Complex systems, such as the formation of oil droplets on mineral surfaces [22], can be simulated and tracked in both time and space, and thermodynamic and dynamic properties [23] can be calculated, which can be directly compared with experimental measurements.

In this study, all MD simulations [34] were performed using the quantum mechanics parameterized COMPASS (Condensed-phase Optimized Molecular Potentials for Atomistic Simulation Studies) III force field [35]. The COMPASS III force field is applicable to a broad range of molecules and polymers and accurately describes multiphase systems such as liquid-liquid equilibrium and was used in this study because we are simulating three-phase wettability models to predict oil in brine on mineral surface contact angles.

2.2 Multiphase LBM simulation

Multiphase numerical simulations are conducted using a lattice Boltzmann method (LBM) solver in a 3D segmented pore space of the chosen rock domain. Unlike the traditional Navier-Stokes equations, the LBM is based on mesoscopic kinetic theory and solves a discrete form of the Boltzmann transport equations [36-40]. The LBM operates locally on a cubic lattice, allowing for highly parallel computational performance [41]. This makes it an excellent choice for simulating porous media applications, which often involve large domains with intricate pore structures. The LBM has been successfully used in a range of porous media applications, including hydrocarbon-bearing rocks [42, 43], gas diffusion layers in fuel cells [44, 45] and porous electrodes in lithium-ion batteries [46, 47].

In this study, the LBM implementation is based on the multiphase model introduced by Shan and Chen [48], which has undergone several improvements to achieve accurate simulations for porous media applications even at coarse resolutions (pore throat of as low as 3 voxels radii) and high viscosity ratios (up to 100) scenarios [41, 49]. The multiphase model considers different particle species to represent separate fluid phases, and the interaction forces between these species determine the inter-component interfacial tension. Consequently, the interfaces between different components are automatically determined once the species' interactions are defined. This eliminates the need for explicit interface tracking methods like volume-of-fluid or level-set approaches, simplifying the simulation process.

To accurately capture the physics of multi-component fluid flow, even at low resolution, the current LBM implementation incorporates triangulated surface elements, known as surfels, in addition to voxel elements [50-52].

These surfels precisely define the boundaries between pores and grains, resulting in accurate flux calculations near boundaries and better accuracy at lower numerical resolutions. Moreover, the utilization of surfels enhances the calculation of local curvature and curvature-based pressure as required for the wettability alteration workflow used in the current work.

2.3 Workflow description

2.3.1 Sample Imaging

As for the digital rock multiphase workflow, a 3D image of a Berea sandstone sample is obtained using x-ray micro-tomography (microCT). Figure 1 shows a sub-volume of the 3D microCT scan oriented perpendicular to the fluid displacement direction. The 3D image went through image pre-processing, including artifact corrections, filtering and subsequent segmentation, with details available in [42].
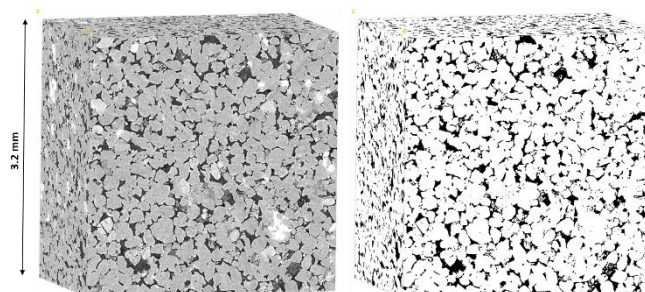

Fig. 1. Sub-volume of a 3D microCT scan for the Berea Sandstone used in this work: Left, original greyscale image, right, segmented image.

The 3D micro-CT image of a Berea sandstone was acquired at 2.0 μm per voxel resolution to ensure good mesh quality for subsequent fluid flow simulation. At this resolution, the resulting 3D model shows sufficient pore connectivity in all three directions, with a total resolved porosity around 14%. The typical range of porosity for this Berea sample is 18~20%. The micro-CT image resolved mostly the relevant connected porosity, while the missing porosity (crevices and clay porosity) does not contribute much to the flow. The pore bottleneck radius, which is defined by the radius of the largest rigid sphere that can be percolated across the 3D pore structure without getting stuck, needs to be large enough to ensure sufficient accuracy of the fluid flow simulation and that requirement is solver specific. In a previously published work [41], it was demonstrated that the LBM solver used for this study can provide accurate results at 3 voxel resolution. The bottleneck radii for this Berea sample model were calculated to be 3.0, 3.6 and 3.2 voxels in the x, y and z directions, respectively.

Afterwards, a representative elementary volume (REV) analysis is performed on the captured image and a subdomain of 500 voxels cubic size is selected for subsequent multiphase analysis. The details of the REV analysis can be found in [21].

2.3.2. Multiphase Simulation Setup

In the selected rock domain, a primary drainage simulation driven by capillary pressure is conducted. Initially, the simulated pore space is fully saturated with water and has a uniform water-wet condition (hydroxylated surface as modeled in the MD simulation) applied throughout. During the primary drainage simulation, the pressure of the oil is gradually increased, leading to the oil displacing the water in the pore space. At each pressure step, once the saturation is converged, capillary pressure is calculated as the pressure difference between the bulk oil and water phases. By bulk we mean the average value in each phase. Concurrently, the wetting condition of the grains dynamically transitions from a water-wet (hydroxylated surface) to an oil-wet (alkylated surface) condition over the course of the simulation. The wetting condition of the grain surface is altered iteratively, where each iteration leads to further oil invasion and incremental oil-wet surface fraction. An illustration of this process is provided in the results section. The simulation setup closely resembles the laboratory process for capillary pressure displacement using a porous plate. In this study, a unique feature of the current lattice Boltzmann method is used – a volume-free, massless numerical membrane that serves as a substitute for the porous plate in laboratory analysis. This numerical membrane effectively addresses computational expenses and potential numerical issues associated with modeling a finely resolved porous plate. For further information regarding the porous plate simulation setup, refer to [21].

2.3.3. Molecular dynamics model

Molecular dynamics (MD) simulations are utilized to compute oil/brine contact angles on α-quartz, the main component of Berea sandstone. Contact angles are highly affected by the surface chemistry of the mineral. When water is more prevalent, the surface of α-quartz will tend to hydroxylate, which results in hydroxyl groups (-OH) covalently bonding to the surface, but in the presence of oil, the surface may undergo alkylation, with alkyl groups (-C_nH_{2n+1}) covalently bonding to the surface. The exchange of these functional groups at the oil/water interface while the fluids displace each other is the molecular mechanism for wettability alteration in reservoir rocks.

Fully-atomistic three-phase wettability models [22] were used to calculate the contact angles of cylindrical oil droplets in brine on α-quartz surfaces. The oil phase was modelled as *n*-octane. The second phase was the brine phase which was modelled as 0.2 wt % NaCl in water. The third phase was the mineral phase, modelled as fully hydroxylated or alkylated α-quartz. The molecular components of the three-phase wettability model are shown in Figure 2.
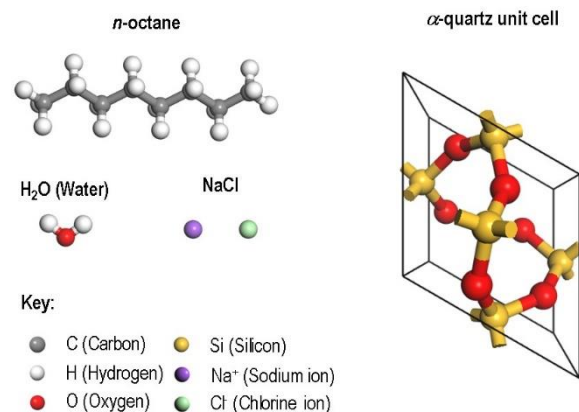

Fig. 2. Molecular representations of components in the three-phase wettability model: n-octane, water, NaCl, and unit cell of α-quartz crystal.

The quartz surfaces were prepared by converting the primitive unit cell of α-quartz to its orthorhombic cell equivalent as described in [53]. A 10x6x6 supercell with dimensions of 4.9 nm x 5.1 nm x 3.8 nm was created, and the (001) surface (the (001) α-quartz surface is known to be the most stable [54]) was cleaved, capping the surface with hydroxyl groups to create the theoretical maximum (9.4 OH/nm^2) [55] hydroxylated surface coverage. However, in nature [56], the hydroxyl surface coverage on α-quartz is 4.6 OH/nm^2, about half of the theoretical maximum, and experimental measurements indicate that alkylation [57] reduces the hydroxylation. Thus, to compare the two extremes, we have alkylated a second α-quartz surface to 4.8 pentyl groups per nm^2, with the remaining coverage being hydroxylated at 4.6 OH/nm^2. For oil droplets, a fully hydroxylated surface is hydrophilic, which will tend to result in a water-wet contact angle (<90°) [55], while a fully alkylated surface will tend to be oil-wet (>90°). The resulting fully hydroxylated and alkylated surfaces were replicated 8 times in the x-direction to create a 39.3 nm x 5.1 nm x 3.8 nm surface in which the oil and brine phases were added on top. The oil phase contained 617 *n*-octane molecules. The brine phase contained 55,824 water and 36 NaCl molecules. The hydroxylated α-quartz mineral phase contained 66,884 atoms, and the alkylated α-quartz mineral phase contained 71,520 atoms. The total system sizes were 259,470 atoms for the fully hydroxylated surface model and 264,106 atoms for the alkylated surface model. The initial box dimensions were approximately 39.3 nm x 5.1 nm x 16.4 nm for both the hydroxylated and alkylated three-phase wettability surface models.

2.3.4. Molecular dynamics simulation setup

Contact angle simulations were performed using all-atom molecular dynamics (MD) simulations of the three-phase wettability models for cylindrical oil droplets on the fully hydroxylated and alkylated α-quartz surfaces. MD simulations were performed in the isobaric isothermic (NPT) ensemble at a referential reservoir condition: 6800 psi and 240 °F. Temperature and pressure were maintained using a

Berendsen thermostat and barostat, respectively. Simulations were run for 5 ns using a 1 fs time step with atomic coordinates recorded every 50 ps. The oil droplets are fully formed within 2 ns, but an additional 3 ns of dynamics were run to confirm that no significant changes occurred to the droplet shape. All intermolecular and intramolecular interactions were modeled using the COMPASS III force field [35], with van der Waals interactions truncated with a cubic spline and a 1.25 nm cut-off. Electrostatic interactions were summed using the Particle-Particle Particle-Mesh (PPPM) method [58].

2.3.5. Wettability alteration

The current workflow involves the integration of molecular and micro-scale fluid simulation data to achieve wettability alteration. Firstly, molecular dynamics simulations are employed to calculate the oil/water contact angle for a fully hydroxylated (water-wet) and alkylated quartz surface (oil-wet). Secondly, utilizing the contact angle inputs obtained
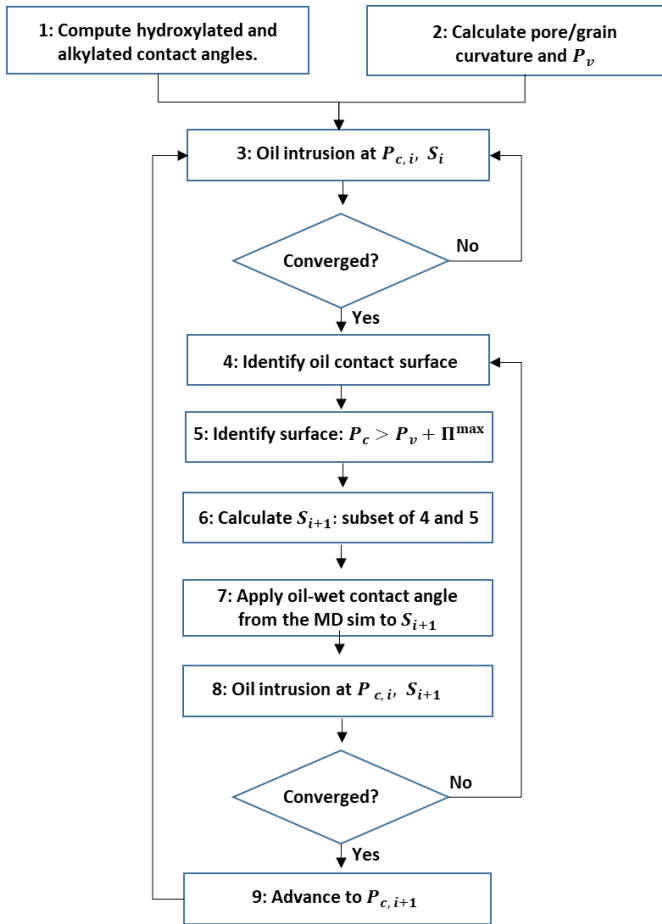

Fig. 3. Molecular dynamics and lattice Boltzmann workflow for wettability alteration.

from the MD simulation, a primary drainage displacement simulation is conducted using the multiphase LBM method.

Figure 3 provides a detailed overview of the workflow implementation. At step-1, water-wet and oil-wet contact

angles are calculated by simulating oil droplet on top of a hydroxyl and alkyl treated quartz surface from the molecular dynamics simulation. We assumed that the increase in capillary pressure during the drainage simulation is not sufficient enough to warrant a significant change in contact angles. Indeed, as evidenced from [59], the degree of pressure change required to see any discernible change in surface tension is a few of orders higher than the capillary pressure change observed in the CFD simulation. Instead of calculating the contact angle variations due to pressure change, we simulated the change in contact angle by modelling changes of functional groups (hydroxyl for water-wet and alkyl for oil-wet) capping the quartz surface. Thus, the MD simulations are performed only once and the computed contact angle values are used as inputs in various pressure stages of CFD simulation. At step-2, the curvature of the pore/grain boundary is calculated at each voxel of the 3d micro-CT image, as
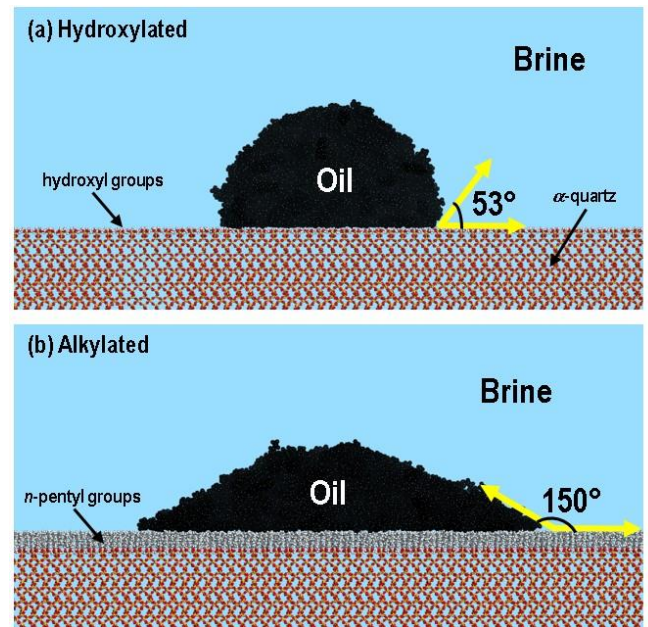

Fig. 4. Oil droplet formation on (a) hydroxylated and (b) alkylated α-quartz surfaces from fully-atomistic three-phase wettability molecular dynamics simulations. Brine (water and NaCl) is explicitly modeled in the simulation but is not shown in the images for better clarity of the oil droplets, which are represented in all black. The blue background is for visualization purposes and has no physical meaning.

described in [21], to incorporate microscale roughness. The curvature based pressure, P_v, is calculated as:

$$P_v = \sigma |\bar{H}| \tag{1}$$

Here, σ and $|\bar{H}|$ represent the interfacial tension and mean curvature of the pore/grain boundary. Note that P_v varies spatially with the curvature of the pore/grain boundary and it is pre-computed before performing the multiphase LBM simulation. In the multiphase LBM simulation (step-3), as the pressure at the oil buffer increases, oil displaces water in the
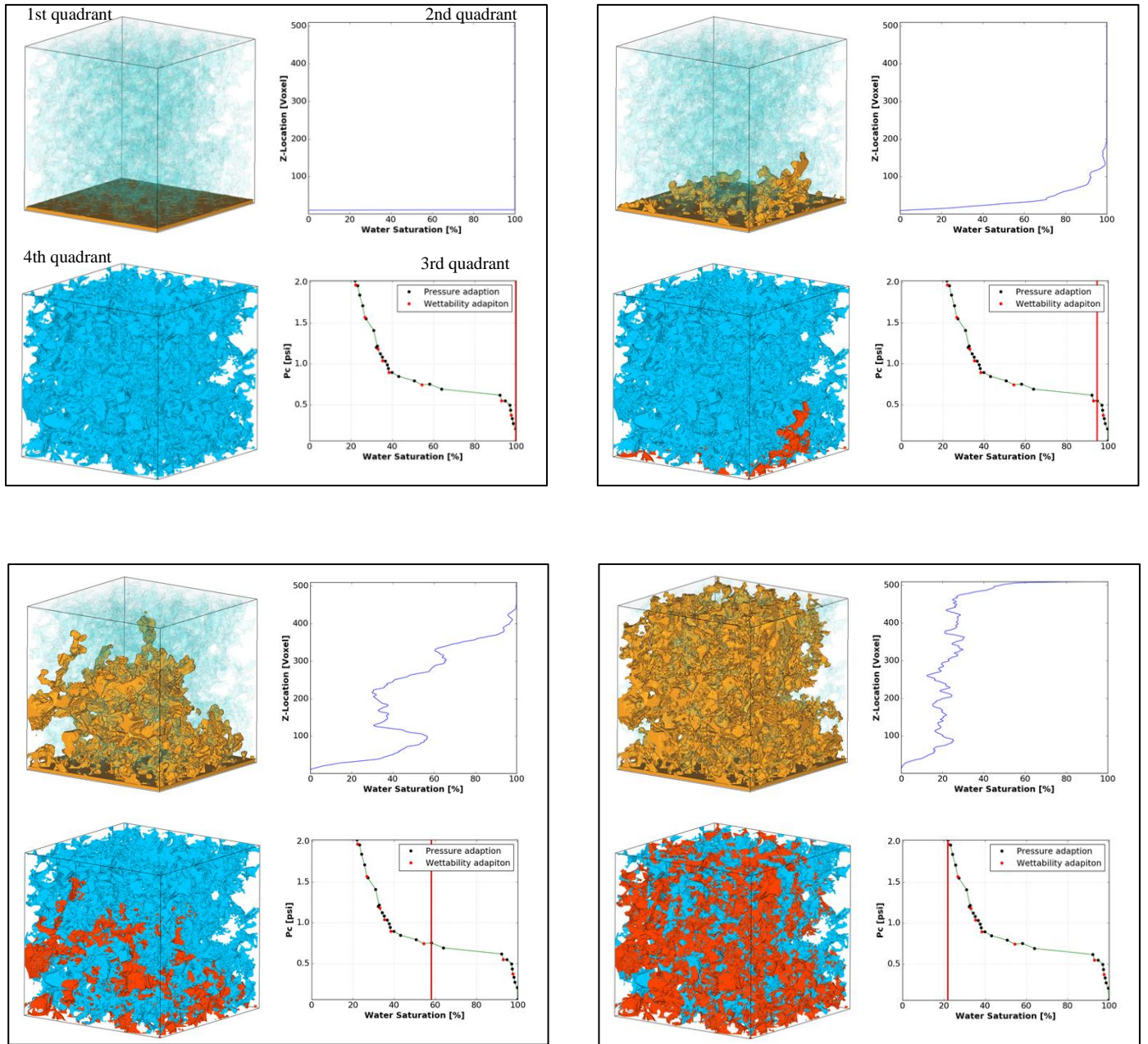
Fig. 5. Various stages of wettability alteration simulation. The 1st quadrant in each figure shows an isosurface of oil, representing oil pore volume (beige) and a volume rendering of water (blue), 2nd quadrant shows the water saturation profile along the flow direction, 3rd quadrant shows capillary pressure versus water saturation curve and 4th quadrant shows oil-wet (red) and water wet (blue) surface within the pore space in 3D.

pore space, where the water-wet contact angle was determined by the MD simulation for the hydroxylated surface. During the first iteration, surface fraction, S, defined as the ratio of oil-wet and total surface area, is set to zero.

Once saturation has reached convergence for a given pressure, the following augmented Young-Laplace equation (in step -5) is used to determine the eligibility of the grain surface in the vicinity of the oil (step-4) for wettability alteration:

$$P_c > P_v + \Pi^{max} \qquad (2)$$

Here, P_c and Π^{max} represent the capillary pressure and maximum disjoining pressure, respectively. The capillary pressure corresponds to the pressure difference between bulk oil/water phases within the pore space and is calculated from the various stages of the CFD simulation as the pressure in oil buffer is increased. The disjoining pressure indicates the pressure needed to rupture the water film for the oil to make contact with the grain surface. According to [16], when oil is pushed against a water-wet flat surface, the capillary pressure resistance caused by pore curvature is absent, but a certain level of pressure is still required for film breakage, known as the disjoining pressure. However, for a curved interface, both

the capillary pressure caused by curvature and the disjoining pressure need to be taken into account. In the current work, the value for the maximum disjoining pressure is assumed to be $5 (10^4)$ Pa, from the available literature [16].

At step-6, the eligible surface fraction for the wettability alteration (S_{i+1}) is calculated by taking a subset of the surface in step-4 and 5, which is later assigned to an oil-wet contact angle as computed from the MD simulations for the alkylated surface (step-7). The simulation is then resumed maintaining the same buffer pressure (step-8). This process allows further redistribution of the invading fluid, and steps 4 to 8 in Fig. 3 are iteratively repeated until convergence in the surface fraction (S) is achieved. Afterwards, the oil pressure is increased to $P_{c,i+1}$ (step-9) and the workflow starts over from step-3.

3 Results and Discussions

3.1 Contact angle calculation

Oil droplet contact angles were measured from the final configurations of the all-atom molecular dynamics three-phase wettability model simulations shown in Figure 4. Contact angles were measured [60] by fitting a circle to where the oil-brine interface meets the solid surface. Measurements were repeated 5 times to calculate averages and standard deviations. The oil droplet contact angle was $53 \pm 2°$ on the fully hydroxylated α-quartz mineral surface, indicating a water-wet condition due to the high concentration of hydroxyl groups (9.4 OH/nm^2) which leads to a hydrophilic interaction between the brine and α-quartz surface. As described in 2.3.3, the alkylated surface contains 4.8 pentyl groups per nm^2 which are covalently bonded to the α-quartz. The alkylated surface has a hydrophobic interaction with the brine, which causes the oil droplet's wettability on the alkylated surface to increase compared to the fully hydroxylated hydrophilic surface. This increased wettability on the alkylated surface results in an oil-wet condition with a contact angle of $150 \pm 4°$. These results are summarized in Table 1.

Table 1. Contact angles calculated from molecular dynamics simulations

	Hydroxylated Surface	Alkylated Surface
Average angle	53°	150°
Standard Deviation	2°	4°

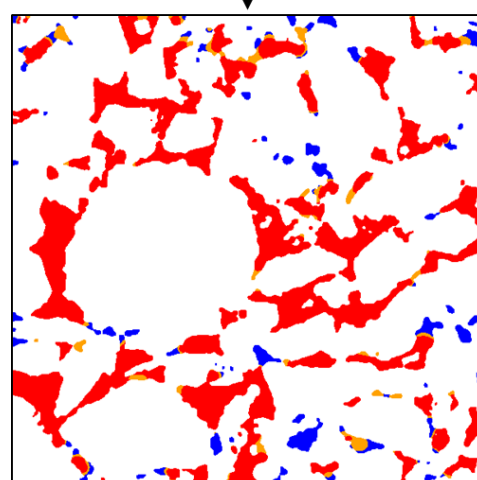## 3.2 Wettability alteration

Figure 5 displays the results of capillary pressure drainage (oil displacing water) simulation in a water-wet Berea sandstone filled with water. General trends of the observed capillary pressure curve are very similar to previously reported experimental and numerical studies. As the oil pressure is increased, oil starts to invade the pore space from the oil buffer. Initially, the water saturation changes are
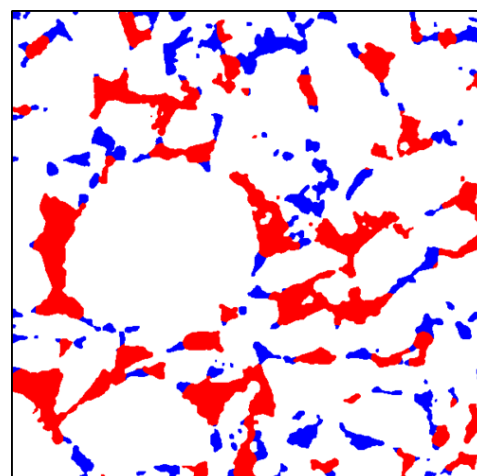
(a) Converged saturation at a given pressure
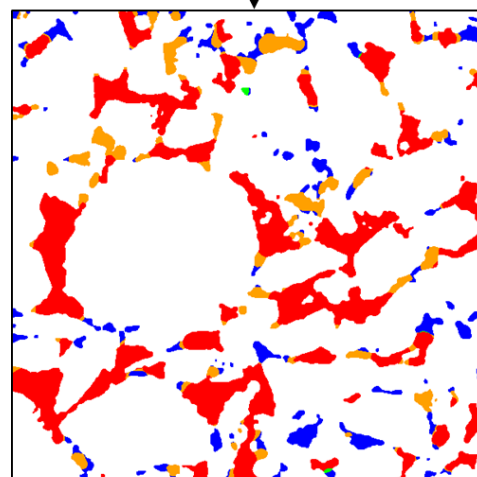
(b) Saturation after 1st wettability alteration

(c) Saturation after 2nd wettability alteration

Fig. 6. Saturation change in the iterative wettability alteration process. Blue, red and orange colors represent the water phase, the oil phase before wettability alteration and the newly intruded oil phase due to wettability alteration, respectively.
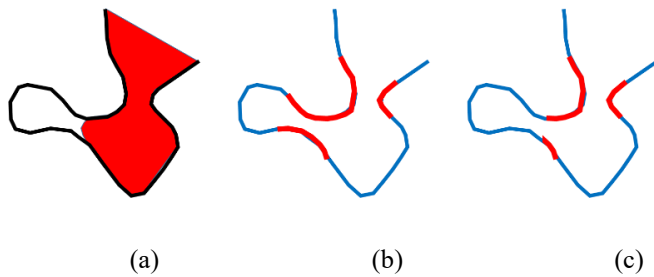
Fig. 7. Determination of wettability alteration eligibility. (a) a pore space partially filled with oil (red), (b) pore/grain boundary that satisfies the Young-Laplace criteria (red) and that does not (blue), and (c) pore/grain boundary after wettability alteration with oil-wet (red) and water-wet (blue) surface.

minimal in response to the increase in oil pressure. However, once the pressure surpasses the capillary pressure imposed by the critical pore throat radius, oil rapidly invades the pore space behind these pore throats, resulting in a phenomenon known as "Haines jump" [61]. It should be noted that not all of the pore space is filled during Haines jumps, particularly during a slow convergence to static equilibrium. In this stage, the phase pressure difference is not significant enough for the non-wetting phase to rapidly invade, and the flow of oil can be described as quasi-static and capillary dominant. In such a scenario, oil droplets can be detached when passing through narrow pore throats, similar to the "Roof snap off" described in [62]. More details of these phenomena can be found in [21]. Once the dominating percolating flow paths are invaded by oil, it starts to displace water in smaller pores at higher pressure slowly. However, most of the remaining water is either trapped in the pore space or coating the grains as a higher pressure thin water film by this time. As a result, the slope of the capillary pressure curve becomes steep again.

Illustrating the current workflow, Figure 5 displays the capillary pressure curve, highlighting the static convergence points after each pressure increment (black) and wettability alteration (red). As described in section 2.3.5, the process ensures that fluid saturation changes due to pressure ramp-up converges in the time domain before a modification to the wetting condition is made. Wettability alteration induces further changes to the overall saturation. In accordance with [21], this phenomenon can be attributed to the slow dynamic impact of wettability alteration, allowing the non-wetting fluid to intrude into very small pores without needing to overcome capillary pressure. Moreover, our proposed molecular mechanism of hydroxyl to alkyl functional group replacement when oil displaces water is consistent with the slow dynamics observed experimentally.

An example of this wettability alteration process is presented in Figure 6, illustrating the iterative convergence of wettability and the resulting fluid saturation. Figure 6 depicts the fluid distribution within a specific plane perpendicular to the overall flow direction. In Figure 6a, oil (red) and water (blue) are present after saturation convergence at a given pressure. Following the alteration of wettability using the

methodology described in section 2.3.5, oil further infiltrates the pore space, which is identified by the orange color in Figure 6b. With the updated fluid distribution, another round of wettability alteration is conducted, resulting in further changes in fluid saturation observed in Figure 6c. In the current workflow, the wetting condition is iteratively modified until both saturation and the surface fraction are converged. Thus, Figure 6 shows that oil can get into smaller pores through an iterative wettability alteration process more effectively than without alteration.

This wettability alteration criteria can be described as an implementation of the augmented Young-Laplace equation, Eq (1), that also accounts for quasi-static changes in fluid saturation. Note that the presence of an oil phase alone is not sufficient for wettability alteration, as it also requires the relationship between local capillary pressure, curvature-based pressure, and maximum disjoining pressure in Eq (1) to be satisfied. Figure 7 illustrates a pore-scale event where a certain pore is partially filled with oil, but depending on the Young-Laplace equation, only a fraction of the oil-contacted grain is altered towards the oil-wet condition.

The current workflow incorporates the consideration of microscale pore shape for wettability alteration by calculating the 3D curvature throughout the entire pore space. As discussed in [63], reservoirs can be classified as mixed-wet large (MWL), mixed-wet small (MWS), or fractional-wet (FW). MWL reservoirs mainly consist of concave pores, with mixed wet conditions observed in the larger pores. In contrast, interestingly, MWS reservoirs consist of convex-shaped pores, where smaller pores exhibit mixed wet characteristics. That study [63] analysed 13 reservoirs from the North Sea oil fields database, with five being classified as MWL, four as MWS, and four as FW.
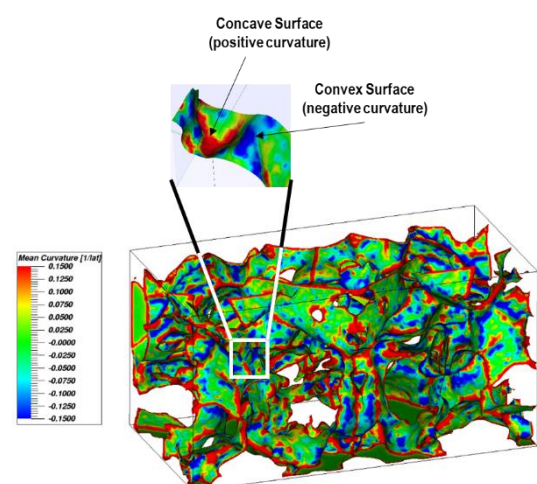

Fig. 8. Calculated mean curvature at pore/grain boundary in one of the simulation subdomains.
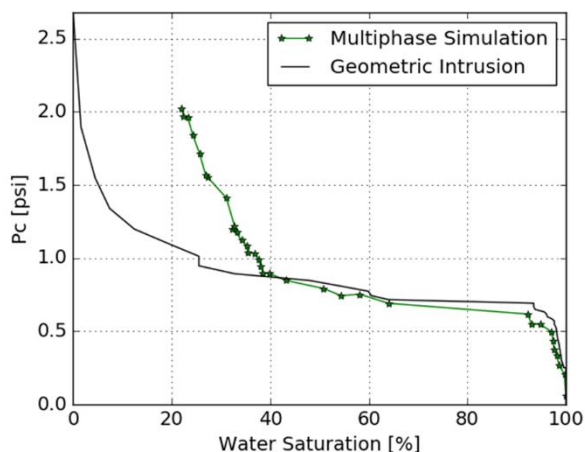
Fig. 9. Comparison of the capillary pressure curve in the multiphase simulation and geometric intrusion process.
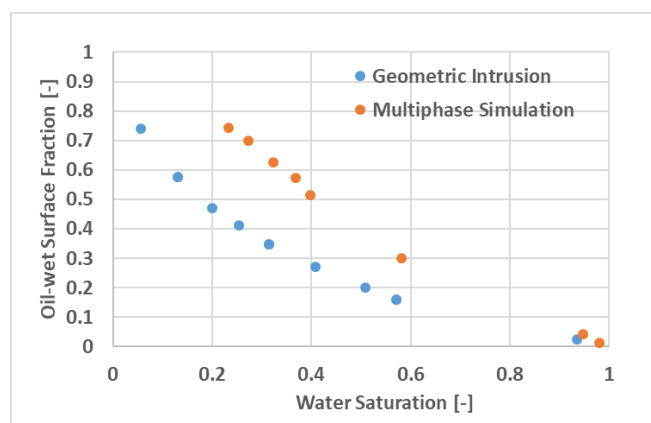

Fig. 10. Oil-wet surface fraction as predicted from the multiphase drainage and geometric MIP analysis.

In the current study, the curvature-based pressure, P_v, is computed as a function of the mean curvature, $|\bar{H}|$, of the pore/grain boundary (Eq. 1). $|\bar{H}|$ values are positive or negative for concave or convex pores, respectively. Figure 8 showcases a mean curvature map in a fraction of the simulated pore space. P_v, calculated from equation (1), is used in equation (2) for surface wettability candidacy. According to equation (2), for a given maximum disjoining pressure (Π^{max}), convex pores are more likely candidates for wettability alteration. Thus, using the augmented Young-Laplace equation and corresponding curvature calculation in the current workflow can potentially explain the wettability characterization of the MWS reservoirs.

Figure 9 compares the drainage capillary pressure curve obtained from the multiphase simulation and an image-based geometric intrusion analysis, which resembles the laboratory procedure of mercury intrusion porosimetry (MIP). The geometric intrusion process employs the inscribed sphere method, where the radius of the sphere corresponds to the applied capillary pressure determined using the Young-

Laplace equation. During the multiphase simulation, approximately 23% of the water becomes trapped at the end of the drainage process. In contrast, the geometric intrusion analysis relies on the connectivity of the oil phase and the size of the pore space, neglecting the connectivity of the water phase. Consequently, this method is unable to predict the presence of the trapped water phase, leading to a discrepancy observed during the late drainage process. However, it is important to note that the capillary entry pressures observed in both methods are very similar.

Figure 10 shows the oil-wet surface fraction obtained from multiphase analysis and the oil-contacted surface fraction predicted by the MIP analysis as a function of water saturation. Note that, even for saturation values where the two capillary pressure curves (Figure 9) are similar, between 40%-80%, the MIP-predicted oil-wet surface fraction (Figure 10) is considerably lower than that obtained from the multiphase simulation. This difference suggests that, in the multiphase simulation that incorporates the Young-Laplace equation (Eq (1)) and a slow dynamic interface advancing scheme during wettability alteration, supported by the molecular mechanism of functional group substitution, oil can penetrate deeper into the smaller pores at a given saturation. In contrast, the oil saturation in the MIP analysis strictly represents the pore space that can be invaded according to the Young-Laplace equation. In the absence of dynamic wettability alteration, the MIP process cannot predict oil intrusion into smaller pores without overcoming capillary pressure first.

4 Conclusion

A numerical wettability alteration process was presented that integrates molecular-driven physicochemical properties with pore-scale capillary flow in order to predict rock wettability under in-situ reservoir conditions. We proposed a molecular mechanism for wettability alteration, which involves the alkylation of mineral surfaces as oil displaces water within the pore space of rock. An iterative workflow for multiphase CFD simulation was presented, which determines the spatial rock wettability distribution as a function of applied capillary pressure and saturation. Inputs to the workflow were contact angles calculated from fully atomistic molecular dynamics models of oil droplets on hydroxylated and alkylated quartz surfaces. Detailed pore-scale events during wettability alteration were examined and compared with an image-based geometric intrusion analysis, which mimics mercury intrusion porosimetry (MIP) virtually.

The developed virtual wettability alteration process achieves a force balance by considering local capillary pressure, disjoining pressure and curvature-based pressure. A detailed description of the slow oil invasion mechanism during wettability alteration has been provided, taking into account pore/grain curvature and its influence on the augmented Young-Laplace equation. Comparison with the virtual MIP analysis reveals that iterative wettability alteration allows oil to invade smaller pores without overcoming capillary pressure. Additionally, the overall oil-wet surface fraction

was found to be significantly higher than that obtained from virtual MIP analysis at a given water saturation. The combination of slow dynamic wettability alteration and curvature effects offers an explanation for the observed wettability conditions in mixed-wet small reservoirs.

Through a synergistic combination of atomistic molecular dynamics and multiphase CFD fluid flow simulations, the presented workflow enables wettability predictions based on first principles numerical simulations. The developed process can serve as a valuable addition to laboratory procedures for determining wettability. Simultaneously, it offers realistic inputs for a range of digital rock workflows, including capillary pressure, relative permeability, and enhanced oil recovery. Consequently, time-constrained projects can now embrace a combination of virtual and laboratory-based wettability assessment, resulting in enhanced uncertainty quantification of the reservoirs. The present work forms the basis for a more detailed analysis of disjoining pressure isotherms. This will be the subject of future work.

List of Symbols and Notations

Symbol	Description
σ	Surface tension coefficient
$|\bar{H}|$	Mean curvature at pore-grain boundary
P_c	Capillary pressure, i.e. pressure difference between bulk oil and water phase
P_v	Curvature based pressure
Π^{max}	Maximum disjoining pressure
S	Surface fraction, i.e, ratio of oil-wet surface to total surface area.
i	A certain iteration within the loop

References

1. W.G. Anderson, "Wettability literature survey-part4: Effects of wettability on capillary pressure," *J Pet Technol* **39,** 1283 (1987)

2. W.G. Anderson, "Wettability literature survey-part 5: The effects of wettability on relative permeability," *J Pet Technol* **39,** 1453 (1987)

3. Q. Lin, B. Bijeljic, S. Berg, R. Pini, M.J. Blunt, S. Krevor, "Minimal surfaces in porous media: Pore-scale imaging of multiphase flow in an altered wettability Bentheimer sandstone", *Phys. Rev. E*, **99,** 6 (2019).

4. M. Rücker , W.-B. Bartels , G. Garfi, M. Shams, T. Bultreys, M. Boone, S. Pieterse, G.C. Maitland, S. Krevor, V. Cnudde, H. Mahani, S. Berg, A. Georgiadis, P.F. Luckham, "Relationship between wetting and capillary pressure in a crude oil/brine/ rock system: From nano-scale to core-scale", *J Colloid Interface Sci.,* **562**, 159(2020)

5. M. Rücker, W.-B. Bartels, K. Singh, N. Brussee, A. Coorn, H. A. van der Linde, A. Bonnin, H. Ott, S. M. Hassanizadeh, M. J. Blunt, H. Mahani, A. Georgiadis, S. Berg, "The effect of mixed wettability on pore-scale flow regimes based on a flooding experiment in Ketton limestone," *Geophys. Res. Lett.* **46,** 3225-3234 (2019).

6. C. McPhee, J. Reed, I. Zubizarreta, "Chapter 7-wettability and wettability tests," *Developments in Petroleum Science,* **64**, 313-345, (2015).

7. G. Garfi, C.M. John, M. Rücker, Q. Lin, C. Spurin, S. Berg, S. Krevor, "Determination of the spatial distribution of wetting in the pore networks of **Error! Bookmark not defined.**", *J Colloid Interface Sci.,* **613**, 786 (2022).

8. G. Garfi, C.M. John, Q. Lin, S. Berg, S. Krevor, "Fluid surface coverage showing the controls of rock mineralogy on the wetting state," *Geophys. Res. Lett.* **47** (8) (2020).

9. S. Foroughi, B. Bijeljic, Q. Lin, A.Q. Raeini, M.J. Blunt, "Pore-by-pore modeling, analysis, and prediction of two-phase flow in mixed-wet rocks," *Phys. Rev. E* **102**, 02330 (2020).

10. Q. Lin, B. Bijeljic, S. Berg, R. Pini, M.J. Blunt, S. Krevor, "Minimal surfaces in porous media: Pore-scale imaging of multiphase flow in an altered wettability Bentheimer sandstone", *Phys. Rev. E*, **99,** 6 (2019).

11. A. Scanziani, K. Singh, M.J. Blunt, A. Guadagnini, "Automatic method for estimation of in situ effective contact angle from X-ray micro tomography images of two-phase flow in porous media", *J. Colloid Interface Sci.* **496**, 51 (2017).

12. W.-B. Bartels, M. Rücker, M. Boone, T. Bultreys, H. Mahani, S. Berg, S.M. Hassanizadeh, V. Cnudde, "Imaging spontaneous imbibition in full Darcy-scale samples at pore-scale resolution by fast X-ray tomography", *Water Resour. Res.,* **55** 7072 (2019).

13. A.M. Alhammadi, A. AlRatrout, K. Singh, B. Bijeljic, M.J. Blunt, "In situ characterization of mixed-wettability in a reservoir rock at subsurface conditions", *Sci. Rep.*, **7,** 10753 (2017).

14. M. Andrew, B. Bijeljic, M.J. Blunt, "Pore-scale contact angle measurements at reservoir conditions using X-ray microtomography", *Adv. Water Resour.*, **68**, 24 (2014).

15. M. Prodanović, W.B. Lindquist, R.S. Seright, "Residual fluid blobs and contact angle measurements from X-ray images of fluid displacement," *XVI International Conference on Computational Methods in Water Resources,* (2006).

16. C.J. Radke, A.R. Kovscek, H. Wong, "A pore-level scenario for the development of mixed wettability in oil reservoirs," SPE 24880, *SPE Ann. Tech Conf. and Exhib.,* Washington, D.C. USA, Oct, 1992.

17. B.V. Derjaguin, E.V. Obukhov, "Anomalous properties of thin polymolecular films V.," Acta Physicochim. URSS, **10**(1), 25-44 (1939a).

18. B.V. Derjaguin, E.V. Obukhov, "Anomalous properties of thin polymolecular films V.," Acta Physicochim. URSS, **10**(2), 153-174 (1939b).

19. S. Iglauer, "CO_2-water-rock wettability: variability, influencing factors, and implications for CO_2 geostorage" *Acc. Chem. Res.*, **50**, 1134−1142, 2017.

20. J.S. Buckley, C. Bousseau, Y. Liu, "Wetting alteration by brine and crude oil: from contact angles to cores," *SPE J.*, **1**, 341-350, 1996.

21. A. Islam, R. T. Salazar, B. Crouse, "Digital rock workflow to calculate wettability distribution in a reservoir rock," SCA 2022-024, *Int. Symp. Soc. Core Analysts,* Austin, TX, USA, (2022).

22. S. Xu, J. Wang, J. Wu, Q. Liu, C. Sun, B. Bai, "Oil contact angles in a water-decane-silicon dioxide system: effects of surface charge," *Nanoscale Research Letters*, **13**, 1-9, 2018.

23. K.E. Gubbins and J.D. Moore, "Molecular modeling of matter: Impact and prospects in engineering," *Ind. Eng. Chem. Res.*, **49**, 3026-3046, 2010.

24. G.J. Martyna, D.J. Tobias, M.L. Klein, "Constant pressure molecular dynamics algorithms," *J. Chem. Phys.*, **101**, 4177-4189, 1994.

25. B.J. Alder and T.E. Wainwright, "Molecular dynamics by electronic computers," In International Symposium on Statistical Mechanical Theory of Transport Processes, Brussels, 1956; Prigogine, I., Ed.; Interscience: New York, 1958.

26. C. Moon, P.C. Taylor, P.M. Rodger, "Molecular dynamics study of gas hydrate formation," *J. Am. Chem. Soc.*, **125**, 4706-4707, 2003.

27. T.F. Headen, E.S. Boek, G. Jackson, T.S. Totton, E.A. Müller, "Simulation of asphaltene aggregation through molecular dynamics: Insights and limitations" *Energy Fuels*, **31**, 1108-1125, 2017.

28. A. Kate, K.K. Sahu, J. Pandey, M. Mishra, P.K. Sharma, "Green catalysis for chemical transformation: The need for the sustainable development" *Curr. Res. Green. Sustain. Chem.*, **5**, 100248, 2022.

29. T. Düren, Y.-S. Bae, R.Q. Snurr, "Using molecular simulation to characterise metal–organic frameworks for adsorption applications," *Chem. Soc. Rev.*, **38**, 1237-1247, 2009.

30. B. Liu and B. Smit, "Comparative Molecular Simulation Study of CO_2/N_2 and CH_4/N_2 Separation in Zeolites and Metal-Organic Frameworks," *Langmuir*, **25**, 5818-5926, 2009.

31. A. Al-Ostaz, W. Wu, A.H.-D. Cheng, C.R. Song, "A molecular dynamics and microporomechanics study on the mechanical properties of major constituents of hydrated cement" *Composites Part B: Engineering*, **41**, 543-549, 2010.

32. G. Javanbakht, M. Sedghi, W. Welch, L. Goual, "Molecular Dynamics Simulations of CO_2/Water/Quartz Interfacial Properties: Impact of CO_2 Dissolution in Water," *Langmuir*, **31**, 5812-5819, 2015.

33. M. Luo, Z.A. Putman, J. Incavo, M.Y. Huang, J.B. McLaughlin, S. Krishnan, "Molecular Simulations and Experimental Characterization of Fluorinated Nitrile Butadiene Elastomers with Low H_2S Permeability," *Ind. Eng. Chem. Res.*, **58**, 14823-14838, 2019

34. BIOVIA, Dassault Systèmes, Materials Studio, 2022, San Diego: Dassault Systèmes, 2022.

35. R.L.C. Akkermans, N.A. Spenley, S.H. Robertson, "COMPASS III: Automated Fitting Workflows and Extension to Ionic Liquids," *Mol. Sim.*, **47**, 540-551, 2021.

36. S. Chen and G. Doolen, "Lattice Boltzmann method for fluid flows," *Annu. Rev. Fluid Mech.*, **30**, 329 (1998).

37. S. Chen, H. Chen, D. Martinez, and W. Mattheus, "Lattice Boltzmann model for simulation of magnetohydrodynamics," *Phys. Rev. Lett.*, **67**, 3776 (1991).

38. H. Chen, S. Chen, W. Matthaeus, "Recovery of the Navier - Stokes equations using a lattice-gas Boltzmann method," *Phys. Rev. A*, **45**, R5339 (1992).

39. Y. Qian, D. d'Humieres, P. Lallemand, "Lattice BGK models for Navier-Stokes equation," *Europhys. Lett.,* **17**, 479 (1992)

40. H. Chen, "Volumetric formulation of the lattice Boltzmann method for fluid dynamics: Basic concept," *Phys. Rev. E*, **58**, 3955(1998)

41. H. Otomo, H. Fan, R. Hazlett, Y. Li, I. Staroselsky, R. Zhang, R., and H. Chen, H., "Simulation of residual oil displacement in a sinusoidal channel with the lattice Boltzmann method," *Comptes Rendus Mécanique*, **343**, 559 (2015).

42. G.R. Jerauld, J. Fredrich, N. Lane, Q. Sheng, B. Crouse, D.M. Freed, A. Fager, and R. Xu, "Validation of a workflow for digitally measuring relative permeability," SPE 188688, *SPE Abu Dhabi*

Int. Pet. Exhib. & Conf., Abu Dhabi, U.A.E., Nov., 2017.

43. H. Andrä, N. Combaret, J. Dvorkin, E. Glatt, J. Han, M. Kabel, Y. Keehm, F. Krzikalla, M. Lee, C. Madonna, M. Marsh, T. Mukerji, E. H. Saenger, R. Sain, N. Saxena, S. Ricker, A. Wiegmann, X. Zhan, "Digital rock physics benchmarks—part II: Computing effective properties," *Comp. Geosci.*, **50,** 33 (2013)

44. J. Wu, J.J. Huang, "Dynamic behaviors of liquid droplets on a gas diffusion layer surface: Hybrid lattice Boltzmann investigation," *J. App. Phys.*, **118,** 044902 (2015)

45. M.A. Safi, N.I. Prasianakis, J. Mantzaras, A. Lamibrac, F.N. Buchi, "Experimental and pore-level numerical investigation of water evaporation in gas diffusion layers of polymer electrolyte fuel cells," *Int J Heat and Mass Trans.,***115**, 238 (2017).

46. L. Martin, P. Benedikt, K. Benjamin, W. Julius, D. Timo, S. Volker, L. Arnulf, "Understanding electrolyte filling of Lithium-ion battery electrodes on the pore scale using the Lattice Boltzmann Method," *Batteries and Supercaps,* **e202200090**, (to be published)

47. D.H. Jeon, "Wettability in electrodes and its impact on the performance of Lithium-ion batteries," *Energy Storage Materials,* **18**, 139 (2019)

48. X. Shan and H. Chen, "Lattice Boltzmann model for simulating flows with multiple phases and components," *Phys Rev E*, **47**, 1815 (1993).

49. H. Otomo, H. Fan, Y. Li, M. Dressler, I. Staroselsky, R. Zhang, and H. Chen, "Studies of accurate multi-component lattice Boltzmann models on benchmark cases required for engineering applications," *Jour. Comp. Sci.*, **17**, 334 (2016).

50. H. Otomo, B. Crouse, M. Dressler, D.M. Freed, I. Staroselsky, R. Zhang, H. Chen, "Multi-component lattice Boltzmann models for accurate simulation of flows with wide viscosity variation," *Computer Fluids,* **172,** 674 (2018)

51. H. Chen, C. Teixeira, and K. Molvig, "Realization of fluid boundary conditions via discrete Boltzmann dynamics," *Int. J. Mod. Phys. C*, **9**, 1281 (1998).

52. B. Crouse, D. M. Freed, N. Koliha, G. Balasubramanian, R. Satti, D. Bale, and S. Zuklic, "A Lattice-Boltzmann based method applied to Digital Rock characterization of perforation tunnel damage," SCA 2016-058, *Int. Symp. Soc. Core Analysts*, Snow Mass, CO, USA., (2016).

53. W.A. Adeagbo, N.L. Doltsinis, K. Klevakina, J. Renner, "Transport processes at α-Quartz–water interfaces: insights from first-principles molecular dynamics simulations," *ChemPhysChem*, **9**, 994-1002, 2008.

54. V.V. Murashov, "Reconstruction of pristine and hydrolyzed quartz surfaces," *J. Phys. Chem. B.*, **109**, 4144-4151, 2005.

55. A. Abramov, A. Keshavarz, S. Iglauer, "Wettability of fully hydroxylated and alkylated (001) α-quartz surface in carbon dioxide atmosphere," *J. Phys. Chem. C*, **123**, 9027-9040, 2019.

56. L.T. Zhuravlev, "The surface chemistry of amorphous silica. Zhuravlev model," *Colloids Surf. A*, **173**, 1-38, 2000.

57. M. Ali, S. Al-Anssari, M. Arif, A., Barifcani, M. Sarmadivaleh, L Stalker, M. Lebedev, S. Iglauer, "Organic acid concentration thresholds for ageing of carbonate minerals: Implications for CO_2 trapping/storage," *J. Colloid Interface Sci.*, **534**, 88-94, 2019.

58. R.W. Hockney, J.W. Eastwood, *Computer simulation using particles*, IOP Publishing: Bristol (1988).

59. B.Y. Cai, J.T. Yang, T.M. Guo, "Interfacial tension of hydrocarbon+ water/brine systems under high pressure," *J. Chem. Eng. Data,* **41,** 493-496 (1996).

60. C.A. Schneider, W.S. Rasband, and K.W. Eliceiri, "NIH Image to ImageJ: 25 years of image analysis," *Nature Methods*, **9**, 671-675, 2012.

61. W.B. Haines, "Studies in the physical properties of soil : the hysteresis effect in capillary properties and the modes of moisture distribution." *J Agric Sci*, **20**, 97 (1930)

62. J.G. Roof, "Snap-Off of oil droplets in water-wet pores," *SPE J.,* 10, 85 (1970)

63. A. Skauge, K. Spildo, L. Høiland, B. Vik, B. Ottesen, " Experimental evidence of different intermediate wetting states," SCA 2004-04, *Int. Symp. Soc. Core Analysts,* Abu Dhabi, UAE, (2004).